

Suppressing neuroinflammation using the near-infrared light emitted by (Sr,Ba)Ga₁₂O₁₉: Cr³⁺ phosphor

Qi Liu,^a Fangmei Yu,^b Hossein Chamkouri,^a Yanguang Guo,^a Ping Chen,^a Bo Wang,^{c,*} Dongwei Liu,^d and Lei Chen^{b,a,e,*}

^aHefei University of Technology, School of Materials Science and Engineering, Hefei, China

^bChinese Academy of Sciences, Brain Cognition and Brain Disease Institute of Shenzhen Institute of Advanced Technology, Shenzhen, China

^cWuyi University, School of Applied Physics and Materials, Wuyi, China

^dSecond Affiliated Hospital of Anhui Medical University, Department of Ophthalmology, Hefei, China

^eIntelligent Manufacturing Institute of Hefei University of Technology, Hefei, China

Abstract. Neurodegenerative diseases, such as Parkinson's and Alzheimer's diseases, affect the elderly worldwide and will become more prevalent as the global population ages. Neuroinflammation is a common characteristic of neurodegenerative diseases. By regulating the phenotypes of microglia, it is possible to suppress neuroinflammation and, in turn, help prevent neurodegenerative diseases. We report a noninvasive photonic approach to regulating microglia from overexcited M1/M2 to the resting M0 phenotype using a special near-infrared (NIR) light emitted by the SrGa₁₂O₁₉:Cr³⁺ phosphor. The absorbance and internal and external quantum efficiencies of the optimal Sr(Ga_{0.99}Cr_{0.01})₁₂O₁₉ phosphor synthesized at 1400°C for 8 h using 1% H₃BO₃ + 1% AlF₃ as flux are 53.9%, 99.2%, and 53.5%; the output power and energy-conversion efficiency of the LED device packaged using the optimal SrGa₁₂O₁₉:Cr³⁺ phosphor driven at 20 mA reach unprecedentedly 19.69 mW and 37.58%, respectively. The broadband emission of the NIR LED device covers the absorption peaks of cytochrome c oxidase well, and the NIR light can efficiently promote the proliferation of microglia, produce adenosine triphosphate (ATP), reverse overexcitation, alleviate and inhibit inflammation, and improve cell survival rate and activity, showing great prospects for photomedicine application.

Keywords: near-infrared light; LED SrGa₁₂O₁₉:Cr³⁺ phosphor; photobiomodulation; neuroinflammation; microglia.

Received Nov. 27, 2023; revised manuscript received Mar. 12, 2024; accepted for publication Apr. 11, 2024; published online May 8, 2024.

© The Authors. Published by SPIE and CLP under a Creative Commons Attribution 4.0 International License. Distribution or reproduction of this work in whole or in part requires full attribution of the original publication, including its DOI.

[DOI: [10.1117/1.APN.3.3.036008](https://doi.org/10.1117/1.APN.3.3.036008)]

1 Introduction

Parkinson's disease (PD) and Alzheimer's disease (AD), also known as senile dementia, are two common neurodegenerative diseases that seriously endanger health and affect the quality of life of the aged.¹ Although some treatments, including medication (such as having levodopa/carbidopa to improve movement symptoms for PD²; and taking acetylcholinesterase inhibitors and NMDA (N-methyl-D-aspartate) receptor antagonists for

AD to improve cognition),³ rehabilitation (such as taking exercises, acupuncture, moxibustion,⁴ and transcranial magnetic stimulation),⁵ and surgery (such as deep brain stimulation)⁶ have been explored, there is no way to fundamentally stop, prevent, suppress, or reverse the degeneration of neurons.^{7,8} An efficient, safe, low-cost, and no-side-effect therapy is desired for the treatment of degenerative diseases, and photobiomodulation is promising.

Photobiomodulation (PBM), also known as low-level laser therapy, was discovered by Dr. Endre Mester at Semmelweis Medical University (Hungary) in 1967, who tried to repeat the experiment described by McGuff to cure malignant tumors

*Address all correspondence to Bo Wang, wangbo312@mails.ucas.ac.cn; Lei Chen, Shanggan2009@qq.com

using a ruby laser.^{9,10} Mester had shaved the backs of mice and implanted a tumor via an incision in the skin.^{9,10} Because the laser power Mester used was far smaller than McGuff's laser, unfortunately, Mester failed to cure tumors, but he observed that the hair growth in the treated mice was much faster than the controls, calling the effect "laser biostimulation."^{9,10} In the past, it was believed that coherent light from a laser was necessary, but as of today, noncoherent light such as that emitted by light-emitting diodes (LEDs) has been proven to be as efficient as lasers in photobiomodulation.^{11,12} Thus, new light sources based on the LED-chip technique and phosphors that can convert LED-chip blue emission into 600 to 1100 nm red and near-infrared (NIR) light are needed for PBM applications, which will also help to extend the application of LEDs.^{13,14}

Deep red light at 670 nm has mostly been explored for PBM applications. However, cellular and animal experimental studies have shown that combining 670 nm red light and NIR light is more effective than 670 nm red light alone for the treatment of neurological disorders.^{15–17} Although the mechanism of PBM has been studied extensively to meet the requirements of precision treatment in modern medicine, there is much space for us to know the function of various wavelengths and understand the cellular, molecular, and tissular mechanisms of PBM.^{12,18}

In pathology, PD has the feature of progressive death of dopaminergic neurons in the substantia nigra pars compacta, associated with the accumulation of alpha-synuclein inclusions, a neuropathological hallmark of PD, called Lewy bodies, in neurons;¹⁹ and the extracellular amyloid- β (A β) plaques deposited in the brain and the presence of intracellular neurofibrillary tangles composed phosphorylated tau protein in neurons are two typical pathological hallmarks of AD, both comprising highly insoluble and densely packed filaments.²⁰ Both AD and PD have multiple pathogenesis, and the exact pathogenesis is currently unclear. However, neuroinflammation is a common pathological feature of neurodegenerative diseases and is characterized by the activation of central nervous system (CNS) microglia, astrocytes, proinflammatory peripheral lymphocytes, and macrophages. Brain inflammation is found in nearly all patients with PD and AD and is associated with increased numbers of glial cells, or gliosis.²¹ Microglia are tissue-resident macrophages of the CNS that play a role in clearing cellular debris, combating infections, and maintaining tissue homeostasis. In addition, microglia play significant roles in neurogenesis and synaptic pruning during neurodevelopmental programs, interacting with neurons and macroglia to provide trophic support, responding to cytokine and metabolic signals, and driving the refinement of functional neuronal circuits.²² Under pathological conditions, microglia are rapidly activated and differentiated into either a pro-inflammatory M1 phenotype, which is neurotoxic, or an anti-inflammatory M2 phenotype, which is neuroprotective.^{23–25} Classically activated (M1-polarized) microglia are accompanied by transcriptional adaptive functional changes, releasing pro-inflammatory factors and toxic substances to kill pathogens, whereas alternatively, activated (M2-polarized) microglia achieve neuroprotective effects by promoting tissue repair and regeneration. Therefore, by regulating microglia phenotype, it is possible to suppress neuroinflammation and, in turn, help delay or inhibit neuron degeneration in PD and AD. In this study, we report on the NIR light emitted by the SrGa₁₂O₁₉:Cr³⁺ phosphor and confirm that NIR light can efficiently promote the proliferation of BV-2 microglia, produce

adenosine triphosphate (ATP), improve cell activity, and regulate the microglia phenotypes of M1/M2 against neuroinflammation.

2 Experiments

The composition and synthesis of (Sr,Ba)Ga₁₂O₁₉:Cr³⁺ phosphor was optimized at variant conditions by two-step solid-state reactions of the raw materials of SrCO₃ (99.00%), BaCO₃ (99.00%), Ga₂O₃ (99.99%), and Cr₂O₃ (99.95%) with the aid of an appropriate amount of flux, where the flux was chosen from the low melting point compounds of H₃BO₃ (99.95%), AlF₃ (98.00%), BaF₂ (99.00%), NH₄F (99.00%), and their combinations. First, stoichiometric raw materials were weighed and ball-milled for 60 min using a benchtop high-energy vibratory ball mill (HF-Kejing, MSK-SFM-3) with a ball-to-raw-material weight ratio of 2:1. Second, the ball-milled raw materials were filled into corundum crucibles, pressed, and calcinated at 1200°C for 3 h in a muffle furnace. After cooling to room temperature, the preferred samples were thoroughly ground using an agate motor, filled into corundum crucibles, and pressed. Next, the samples were fired at 1300°C to 1450°C for 4 to 12 h in a muffle furnace under ambient air conditions. After cooling to room temperature, the fired samples were ground, washed, sieved, and dried at 120°C to obtain the final products. From these, one sample with optimal properties was selected to package LED devices by coating a mixture of phosphor and high-reflectivity transparent silica on a blue chip, which was fixed on a 2835 holder with 450 nm emission.

The phase of the phosphors was characterized using an X-ray diffractometer (Rigaku, Dmax-III A), the morphology was examined using a tungsten filament scanning electron microscope (SEM) (JSM-6490LV), the absorption spectra were collected using the UV-Vis-NIR spectrophotometer (Shimadzu, UV3600), the excitation and emission spectra were monitored using a fluorescence spectrometer (Hitachi, F4600), and quantum efficiency was measured with an absolute photoluminescence quantum yield measurement system (Hamamatsu, Quantaury-QY plus C13534-31). The optical and electronic properties of the as-packaged LED devices were tested using a high-precision array radiometer (Everfine, HAAS-2000) equipped with a 0.75 m integrating sphere.

The BV-2 microglia (SAIOS) were cultured in Dulbecco's modified eagle medium (DMEM) basal medium with 10% fetal bovine serum (FBS), 1% glutamine, and 1% P/S penicillin-streptomycin in 95% air and 5% CO₂ in an incubator at a constant temperature of 37°C. After the cell density reached 70% to 90% and stable passages, the cells were transferred to 96-well plates for light experiments. The experiments were divided into four groups: (1) no light (control group, in a black environment); (2) NIR light (each time radiating with the NIR light continuously for 15 min within 1 h and repeated five times each day, which lasts for four and a quarter hours, using the NIR LED devices packaged with the SrGa₁₂O₁₉:Cr³⁺ phosphor as above, with the power density of 10 mW/cm²); (3) white light and the NIR light alternatively (15 min NIR + 45 min white light + 15 min NIR + 45 min white light + 15 min NIR + 45 min white light + 15 min NIR, in total, radiating with 180 min white light and 75 min NIR light for each day which lasts for four and a quarter hours, with the power density of white and NIR light in terms of 3 W/cm² and 10 mW/cm², respectively); (4) white light (radiating with ordinary lamp of white LED light source continuously for 4 h each day, with a power density of 3 W/cm²). Among them, the black

environment in the control group was not given any light treatment, and both the ordinary white LED light source and the NIR light source were 3 cm away from the BV-2 microglia, and the power density was as shown above. The absorbance of each group was quantified using a methylthiazole tetrazolium (MTT) (Beyotime, C0009S) assay kit and an enzyme-linked immunosorbent assay (Spectrophotometer, 1510-01314) to quantify the degree of microglia proliferation. The adenosine 5'-triphosphate (ATP) production in each group was quantified using a Cell Titer Glo luminescence assay (Beyotime, C0065S) to test microglial cell activity (Promega, GM2000). The M1/M2 phenotype of microglia induced by stimulation of various types of light was determined by semiquantitative methods using CD14 (Proteintech, 17000-1-AP) and CD16 (Proteintech, 16559-1-AP) immunofluorescence staining (LightCycler 96). There, the procedure of immunofluorescence staining was as follows: 1×10^5 BV-2 microglial cells in good condition were inoculated into the sterile cell crawler in 24-well plate, 24 h later, according to the experimental grouping to the different light environments for light treatment, the end of the light carefully washed twice with phosphate-buffered saline (PBS), and the cells in each well were fixed for 15 min at room temperature by adding 1 mL of 4% paraformaldehyde; subsequently, the cells were washed three times with PBS (each time 5 min), and the cells were permeabilized for 20 min at room temperature by adding 1 mL of 0.5% Triton X-100 (995 μ l PBS + 5 μ l Triton X-100 preparation) permeabilized cells at room temperature for 20 min; PBS was washed three times (5 min each time), 1 mL 10% FBS was added to close the cells at room temperature for 30 min, and then pipetted the sealing solution, added 200 μ l primary antibody directly, and incubated in the refrigerator at 4°C overnight, with the concentration of the primary antibody as follows: CD14 the primary antibody concentration was CD14 (1:200) and CD16 (1:400). On the following day, the sample was rewarmed at room temperature for 30 min, washed with PBS for three times (5 min each time), and then incubated with 200 μ l of the secondary antibody (1:100) of the corresponding species for 1 h, then washed with DAPI for 5 min, and then washed with PBS for three times (5 min each time), and then added with antifluorescent quencher and sealed with fingernail polish, and then the images were captured. The images were quantitatively analyzed using Image J Software. Meanwhile, the results of immunofluorescence staining, MTT test, and ATP test were also analyzed for statistical significance, and three samples were taken for each statistical result in order to take the mean value, and the experiment was repeated twice.

3 Results and Discussion

To obtain a phosphor with optimal luminescence performance, the synthesis was systematically optimized in terms of the reaction temperature, reaction time, reaction fluxes, and Cr³⁺ concentration. Therefore, we synthesized a series of (Sr, Ba)Ga₁₂O₁₉: Cr³⁺ phosphors.

The emission spectra in Figs. 1(a) and 1(b) show that the best reaction temperature and time are 1400°C and 8 to 10 h, respectively, for the synthesis of the SrGa₁₂O₁₉:Cr³⁺ phosphor. The flux played an effective role in lowering the reaction temperature, promoting the diffusion of activators into the host, and improving the morphology of the phosphor particles. With respect to the single component fixed at 2%, the effect of H₃BO₃ on improving the luminescence was much better than that of BaF₂, NH₄F, and AlF₃ [Fig. S1(a) in the [Supplementary Material](#)].

Further studies on the combination of various low-melting point compounds showed that 1% H₃BO₃ + 1% AlF₃ was the most effective [Fig. 1(c)]. Figure 1(d) shows that the optimal concentration range of Cr³⁺ doped is $x = 0.010$ to 0.015 for Sr(Ga_{1-x}Cr_x)₁₂O₁₉. The relative emission intensity of the SrGa₁₂O₁₉:Cr³⁺ phosphors as a function of reaction temperature, time, fluxes, and Cr³⁺ concentration in Figs. 1(a)–1(d) is supported by the excitation spectra in Figs. 2(a)–2(d). For more details on the optimization of the fluxes, see Figs. S1(a) and S1(b) in the [Supplementary Material](#).

Although SrGa₁₂O₁₉:Cr³⁺ and BaGa₁₂O₁₉:Cr³⁺ have the same crystal structure, they exhibit significantly different luminescence properties [Figs. 1(e) and 1(f) and Figs. S1(c) and S1(d) in the [Supplementary Material](#)]. We think it is mainly caused by different site occupations of Cr³⁺ in these two compounds in addition to the crystal field effect, as confirmed by exciting with a variant wavelength in measuring emission spectrum [Figs. S1(c) and S1(d) in the [Supplementary Material](#)] and monitoring at different peaks in measuring excitation spectra [Figs. 2(e) and 2(f)]. In Figs. S1(c) and S1(d) in the [Supplementary Material](#), the emission peak of SrGa₁₂O₁₉:Cr³⁺ at 768 nm mainly comes from the lower-energy center of Cr³⁺ and presents highly efficient luminescence; while the emission peak at 730 nm of BaGa₁₂O₁₉:Cr³⁺ mainly comes from the higher-energy center of Cr³⁺ and presents poorly efficient luminescence. With more than 15% mole ratio of Sr replaced by Ba, i.e., $y \geq 0.15$, the luminescence intensity of (Sr_{1-y}Ba_y)Ga₁₂O₁₉:Cr³⁺ decreases significantly with an increase of y value. However, the luminescence intensity remains relatively stable when with no more than 10% mole ratio of Ba doped into SrGa₁₂O₁₉:Cr³⁺ and realizes the emission band broadens. As can be found from the normalized emission spectra in Fig. 1(f), the full width at half-maximum (FWHM) of the emission spectrum of (Sr_{0.9}Ba_{0.1})Ga₁₂O₁₉:Cr³⁺ is about 5 nm wider than that of SrGa₁₂O₁₉:Cr³⁺.

The X-ray diffraction (XRD) examination (Fig. S2 in the [Supplementary Material](#)) demonstrated that a high-purity SrGa₁₂O₁₉ phase was obtained in this study. Since the radius of Cr³⁺ is larger than Ga³⁺, as expected with the Bragg Law, the shift of diffraction peaks toward a small angle as a function of Cr³⁺ increase in Sr(Ga_{1-x}Cr_x)₁₂O₁₉ is observed in Fig. 3(a), which presents the amplified XRD pattern of typical peaks of the (107) and (114) planes at 2θ 32.5 deg to 32.9 deg and 34.5 deg to 34.9 deg, respectively. This shift further indicates that the activator Cr³⁺ entered the SrGa₁₂O₁₉ host well. The crystallinity of the XRD in Fig. 3(b) suggests that the combination of 1% H₃BO₃ + 1% AlF₃ as a flux is much better than the other conditions, including the same quantity of H₃BO₃ individually and H₃BO₃ combined with NH₄F or BaF₂. The clear profile of the phosphor particles was observed from the SEM picture in Figs. 3(c)–3(f). A comparison between Figs. 3(c) and 3(d) shows that the phosphor particles synthesized with flux [in Fig. 3(d)] are relatively larger and more regular than those synthesized without flux [in Fig. 3(c)]. From the amplified SEM picture in Fig. 3(c), the agglomerated particle, which consisted of many small particles, could be clearly distinguished. Nevertheless, with the aid of the flux, the small particles merged into a larger one, as shown in Fig. 3(d), for which the vanished grain boundaries helped improve the luminescence. These phenomena explain the active effect of the 1% H₃BO₃ + 1% AlF₃ flux on improving the luminescence of the SrGa₁₂O₁₉:Cr³⁺ phosphor.

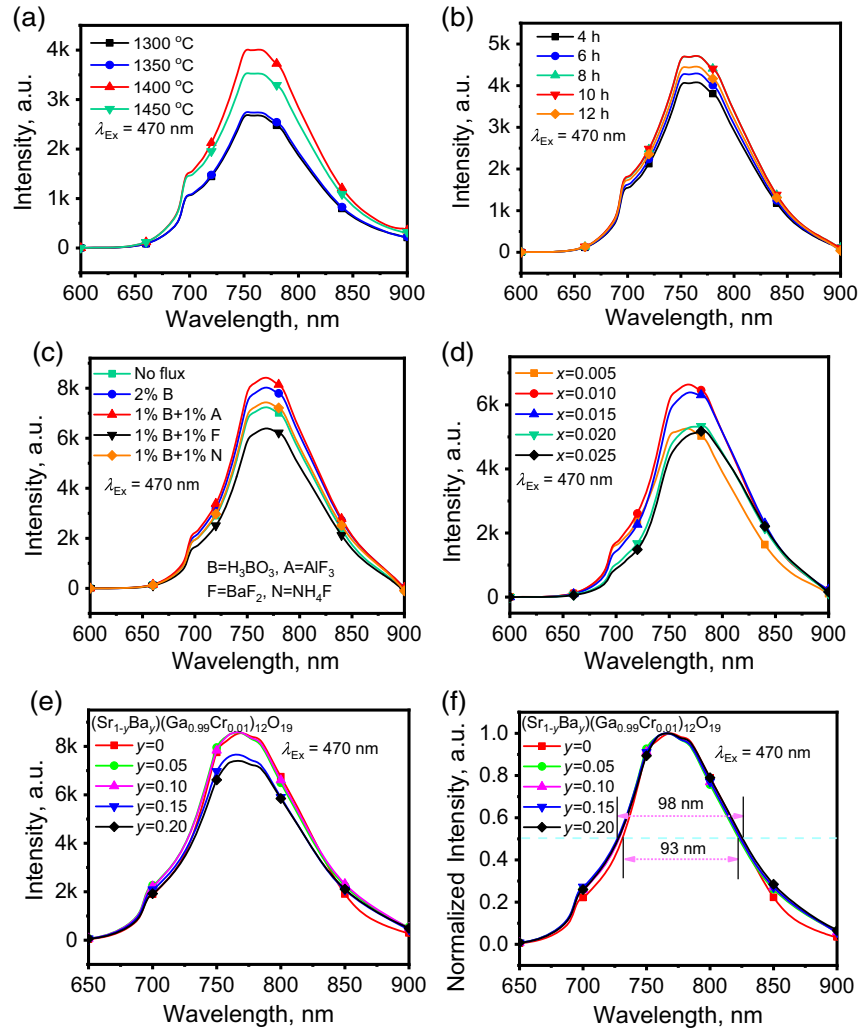


Fig. 1 Emission spectra of $(\text{Sr}_{1-y}\text{Ba}_y)(\text{Ga}_{1-x}\text{Cr}_x)_{12}\text{O}_{19}$ phosphors, synthesized at different conditions and excited with 470 nm. (a) Synthesized at 1300°C, 1350°C, 1400°C, and 1450°C for 4 h with $x = 0.01$ for $\text{Sr}(\text{Ga}_{1-x}\text{Cr}_x)_{12}\text{O}_{19}$; (b) synthesized at 1400°C for 4, 6, 8, 10, and 12 h with $x = 0.01$ for $\text{Sr}(\text{Ga}_{1-x}\text{Cr}_x)_{12}\text{O}_{19}$; (c) synthesized at 1400°C for 8 h with $x = 0.01$ and assisted with variant fluxes for $\text{Sr}(\text{Ga}_{1-x}\text{Cr}_x)_{12}\text{O}_{19}$; (d) synthesized at 1400°C for 8 h with $x = 0.005, 0.010, 0.015, 0.020,$ and 0.025 for $\text{Sr}(\text{Ga}_{1-x}\text{Cr}_x)_{12}\text{O}_{19}$; (e) synthesized at 1400°C for 8 h with $y = 0, 0.05, 0.10, 0.15,$ and 0.20 for $(\text{Sr}_{1-y}\text{Ba}_y)(\text{Ga}_{0.99}\text{Cr}_{0.01})_{12}\text{O}_{19}$; (f) the normalized spectra of (e).

The $\text{SrGa}_{12}\text{O}_{19}$ host has a hexagonal symmetry with the $P63/mmc(194)$ space group. In the host, there are five sites of Ga atoms, which form three types of coordination, i.e., the six-coordinated Ga^{I} , Ga^{IV} , and Ga^{V} with O forming an octahedron of $[\text{Ga}^{\text{I}}\text{O}_6]$, $[\text{Ga}^{\text{IV}}\text{O}_6]$, and $[\text{Ga}^{\text{V}}\text{O}_6]$; the five-coordinated Ga^{II} with O forming a hexahedra $[\text{Ga}^{\text{II}}\text{O}_5]$; and the four-coordinated Ga^{III} with O forming a tetrahedra $[\text{Ga}^{\text{III}}\text{O}_4]$, as shown in Figs. 4(a) and 4(b). Due to the too-small interstice, Cr^{3+} cannot take the site of Ga^{3+} in the $[\text{Ga}^{\text{II}}\text{O}_5]$ hexahedra and the $[\text{GaO}_4]$ tetrahedra. However, Cr^{3+} possibly occupies the center of Ga^{3+} in the three-type $[\text{GaO}_6]$ octahedra. Further study on the site occupation of Cr^{3+} in the $\text{SrGa}_{12}\text{O}_{19}$ host also confirmed that Cr^{3+} mainly takes the place of the Ga^{I} , Ga^{IV} , and Ga^{V} sites, as shown in Fig. 4(c) and Table S1 in the [Supplementary Material](#), suggesting that Cr^{3+} possesses three different coordination environments. Owing to the multiple occupations of Cr^{3+} in the $\text{SrGa}_{12}\text{O}_{19}$ lattice, the superbroad band

of $\text{SrGa}_{12}\text{O}_{19}:\text{Cr}^{3+}$ emission spectra was observed, as shown in Fig. 1, whose FWHM was ~ 102 nm. According to the Tanabe-Sagano diagram shown in Fig. 4(d), the broad mission band of the $\text{SrGa}_{12}\text{O}_{19}:\text{Cr}^{3+}$ phosphor with a peak at ~ 760 nm in Figs. 1(a)–1(d) was attributed to the ${}^4\text{T}_2({}^4\text{F})\text{-}{}^4\text{A}_2({}^4\text{F})$ transition of Cr^{3+} .^{26–28} In addition, a minor peak that overlapped with the broad band at 695 nm was assigned to the spin-forbidden ${}^2\text{E}_g\text{-}{}^4\text{A}_2({}^4\text{F})$ transition of Cr^{3+} .^{26–28} In Figs. 2(a)–2(d), the excitation bands at 300–360 nm were assigned to the host of $\text{SrGa}_{12}\text{O}_{19}$, and the broad excitation bands at 400–500 nm and 550–650 nm were attributed to the ${}^4\text{A}_2({}^4\text{F})\text{-}{}^4\text{T}_1({}^4\text{F})$ and ${}^4\text{A}_2({}^4\text{F})\text{-}{}^4\text{T}_2({}^4\text{F})$ transitions, respectively.^{26–28}

In theory, the Stokes shift, crystal field stability energy (Dq), Racah parameter (B), and Dq/B ratio in the $\text{Sr}(\text{Ga}_{1-x}\text{Cr}_x)_{12}\text{O}_{19}$ ($x = 0.005, 0.010, 0.015, 0.020,$ and 0.025) phosphors were calculated according to the following equations by combining them with the emission spectra in Fig. 1(d).^{29,30}

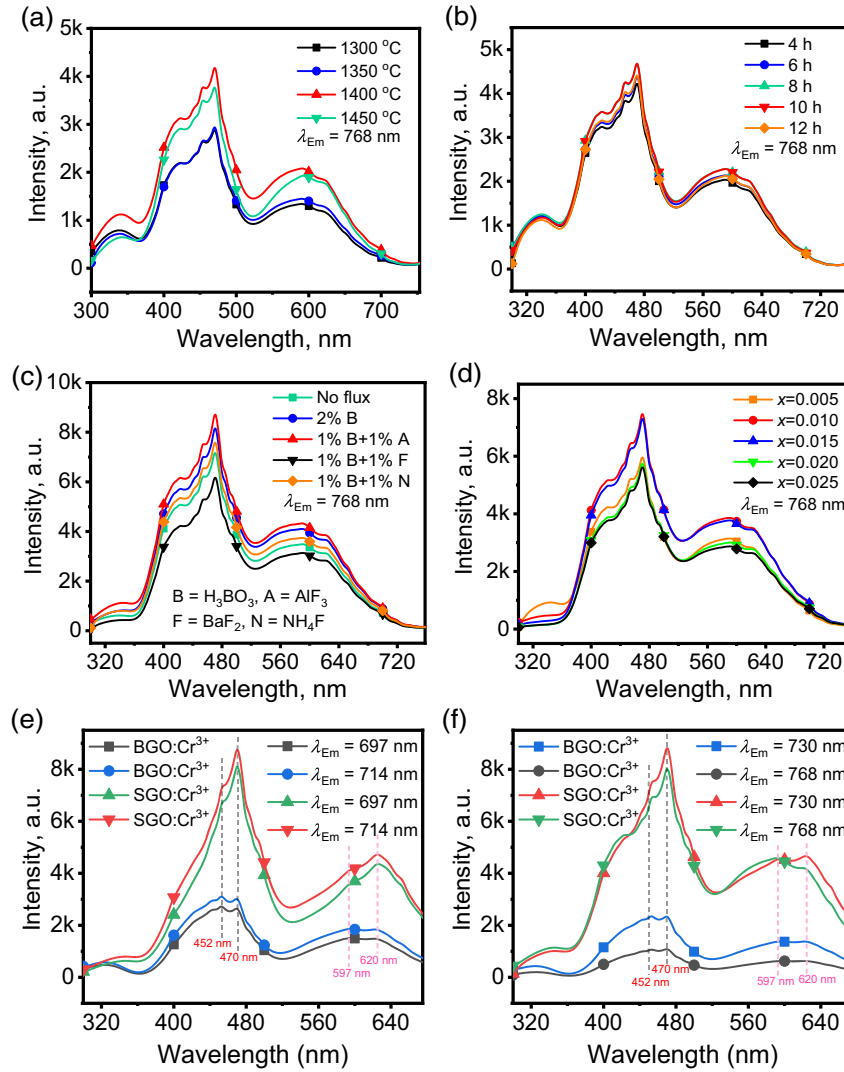


Fig. 2 Excitation spectra of $(\text{Sr}_{1-y}\text{Ba}_y)(\text{Ga}_{1-x}\text{Cr}_x)_{12}\text{O}_{19}$ phosphors, synthesized at different conditions and obtained by monitoring the emission at 768 nm. (a) Synthesized at 1300°C, 1350°C, 1400°C, and 1450°C for 4 h with $x = 0.01$; (b) synthesized at 1400°C for 4, 6, 8, 10, and 12 h with $x = 0.01$; (c) synthesized at 1400°C for 8 h with $x = 0.01$ and assisted with variant fluxes; (d) synthesized at 1400°C for 8 h with $x = 0.005, 0.010, 0.015, 0.020,$ and 0.025 ; (e), (f) $\text{Ba}(\text{Ga}_{0.99}\text{Cr}_{0.01})_{12}\text{O}_{19}$ ($\text{BGO}:\text{Cr}^{3+}$) and $\text{Sr}(\text{Ga}_{0.99}\text{Cr}_{0.01})_{12}\text{O}_{19}$ ($\text{SGO}:\text{Cr}^{3+}$) synthesized at 1400°C for 8 h (e) by monitoring the emission at 697 and 714 nm and (f) by monitoring the emission at 730 and 768 nm.

$$\alpha = \frac{E(^4A_2 - ^4T_1) - E(^4A_2 - ^4T_2)}{Dq}, \quad (1)$$

$$10Dq = E(^4A_2 - ^4T_2), \quad (2)$$

$$\frac{Dq}{B} = \frac{15(\alpha - 8)}{(\alpha^2 - 10\alpha)}. \quad (3)$$

As the calculation results are shown in Table 1, the Stokes shift increased, Dq decreased, and the Dq/B ratio decreased as Cr^{3+} increased from $x = 0.005$ to 0.025 , indicating that the crystal field intensity decreased gradually with increasing Cr^{3+}

concentration. Remarkably, this conclusion is consistent with the shift in the XRD diffraction peaks toward a big angle with increasing Cr^{3+} . The mechanism of the intensified crystal field could explain the continuous shift in the emission peaks of $\text{Sr}(\text{Ga}_{1-x}\text{Cr}_x)_{12}\text{O}_{19}$ from 766 to 783 nm, along with Cr^{3+} increasing from $x = 0.005$ to 0.025 , as seen from the normalized emission in Fig. S3(a) in the [Supplementary Material](#).

The relative intensity of the $\text{Sr}(\text{Ga}_{1-x}\text{Cr}_x)_{12}\text{O}_{19}$ ($x = 0.005, 0.010, 0.015, 0.020,$ and 0.025) emission, obtained by integrating from 650 to 900 nm in Fig. 1(d), was plotted in Fig. S3(b) in the [Supplementary Material](#). The mechanism of concentration quenching was concluded by calculating using the following equation:^{31,32}

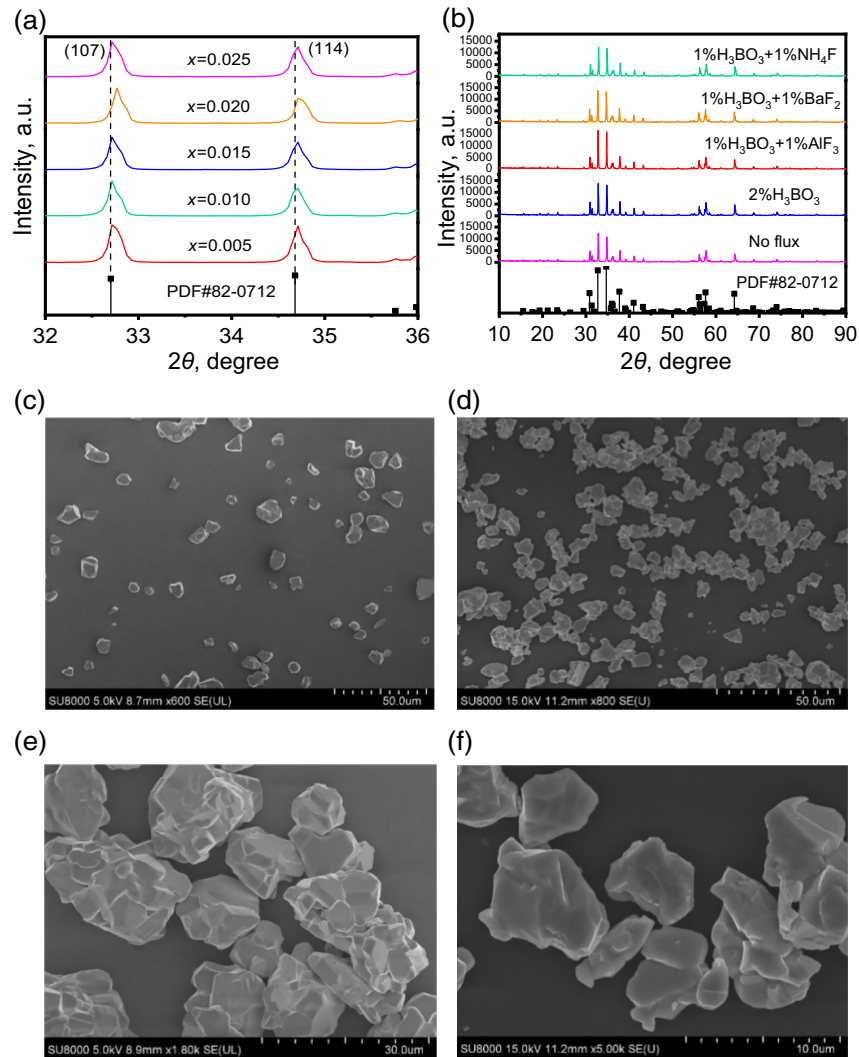


Fig. 3 Crystal structures and morphologies of Sr(Ga_{1-x}Cr_x)₁₂O₁₉ phosphors. (a) XRD patterns of the phosphor synthesized at 1400°C for 8 h with $x = 0.005, 0.010, 0.015, 0.020,$ and 0.025 ; (b) XRD patterns of the phosphor synthesized at 1400°C for 8 h with $x = 0.01$ and assisted with variant fluxes; (c), (e) SEM pictures of the phosphor synthesized at 1400°C for 8 h with $x = 0.01$ and without flux, and the same phosphor by magnified different times for (c) and (e); (d), (f) SEM pictures of the phosphor synthesized at 1400°C for 8 h with $x = 0.01$ and with aid of 1% H₃BO₃ + 1% AlF₃ flux, and the same phosphor by magnified different times for (d) and (f).

$$\frac{I}{x} = K \left[1 + \frac{\beta(x)Q}{3} \right]^{-1}, \quad (4)$$

where I represents emission intensity, x is the activator concentration, K and β are the constants for a given matrix lattice under the same excitation conditions, and Q is the constant for multipole interactions, corresponding to Q values equal to 3, 6, 8, or 10 for the nearest-neighbor ion, dipole–dipole, dipole–quadrupole, or quadrupole–quadrupole interactions, respectively.^{31,32} Because the strongest luminescence appeared at $x = 0.01$, the concentration quenching effect was considered. The relationship between $\lg I/x$ and $\lg x$ within $x = 0.01$ and $x = 0.025$, as shown in the inset in Fig. S3(b) in the [Supplementary Material](#), is approximately linear with a slope of ~ 0.98 , which in turn yields $-Q/3 = -0.98$; therefore, $Q = 2.94 \approx 3$. Hence, we can conclude that the concentration quenching of the SrGa₁₂O₁₉:Cr³⁺

luminescence is mainly caused by the energy transfer between the near-neighbor Cr³⁺ ions in the SrGa₁₂O₁₉ host.

The thermal stability of the luminescence is crucial for phosphor application in LEDs. As shown in Fig. 5(a) and Fig. S4(a) in the [Supplementary Material](#), the luminescence of the optimal phosphor at 150°C maintains 97.34% of that at room temperature, exhibiting excellent thermal stability of luminescence. Evaluated from the integrated intensity of luminescence [Fig. S4(b) in the [Supplementary Material](#) and the inset in Fig. 5(a)], the activation energy was estimated at 0.23 eV, which is smaller than the previously reported value of ~ 0.266 eV by Liu et al.³³

After systematic optimization, the absorbance, internal quantum efficiency (i.e., PLQY), and external quantum efficiency (i.e., EQE) of the Sr(Ga_{0.99}Cr_{0.01})₁₂O₁₉ phosphor, which was synthesized at 1400°C for 8 h using 1% H₃BO₃ + 1% AlF₃

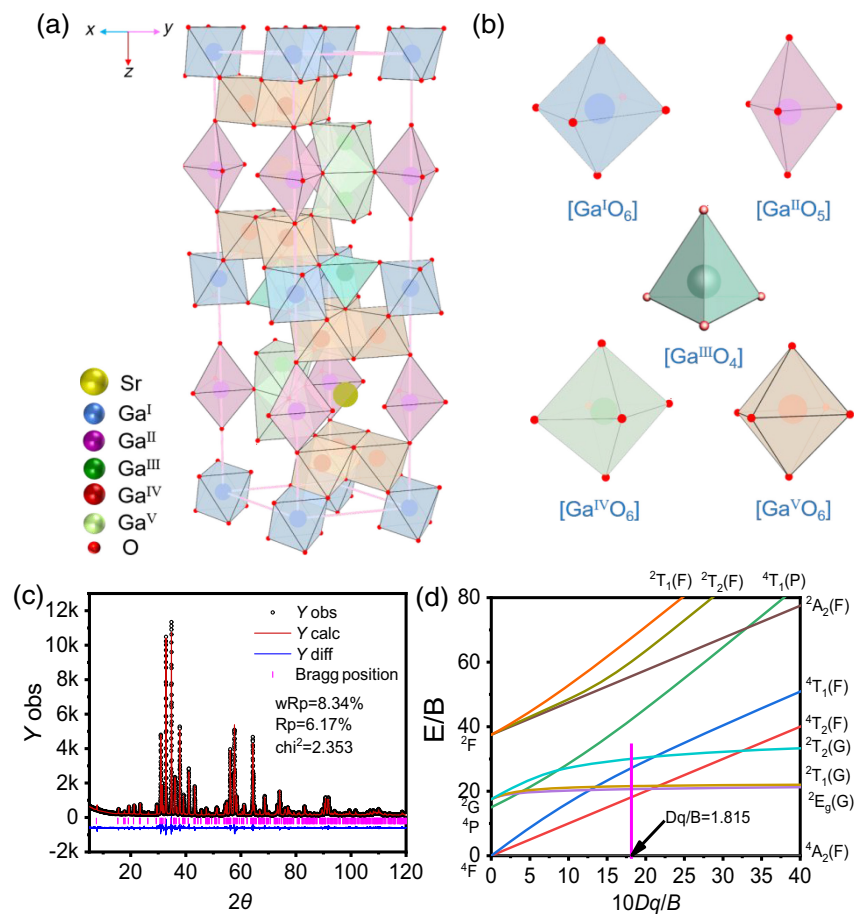


Fig. 4 Crystal structure and luminescence mechanism of SrGa₁₂O₁₉:Cr³⁺ phosphor. (a) The three-dimensional structure of the SrGa₁₂O₁₉ host, (b) the polyhedral coordination of five sites of Ga atoms in the host; (c) the structure refinement of XRD pattern on the site occupation of Cr³⁺ in SrGa₁₂O₁₉ host; (d) the Tanabe–Sugano schematic diagram of Cr³⁺ in sixfold coordination.

Table 1 The Stokes shift, crystal field parameter Dq , and Racah parameter B of Sr(Ga_{1-x}Cr_x)₁₂O₁₉ ($x = 0.005$ to 0.025).

$x\text{Cr}^{3+}$	Stokes shift (cm ⁻¹)	Dq (cm ⁻¹)	B (cm ⁻¹)	Dq/B
0.005	3894.32	1305.48	716.12	1.823
0.010	3828.32	1302.08	717.40	1.815
0.015	3962.14	1298.70	718.71	1.807
0.020	4145.05	1280.41	727.09	1.761
0.025	4161.43	1278.77	727.81	1.757

as flux, are 53.9%, 99.2%, and 53.5%, respectively, as shown in Fig. 5(b). In general, the values reported in this study significantly exceeded those previously reported by Liu et al., which were 45.8%, 98.2%, and 45% for the absorbance, PLQY, and EQE, respectively.³³ Liu et al. made pioneering and unprecedented progress on this phosphor.³² As shown in Fig. S5 in the [Supplementary Material](#), by plotting the normalized emission and excitation of the Sr(Ga_{0.99}Cr_{0.01})₁₂O₁₉ phosphor together, the overlap between them is very small, which explains the highly efficient luminescence of the SrGa₁₂O₁₉:Cr³⁺ phosphor.

The optimal phosphor of Sr(Ga_{0.99}Cr_{0.01})₁₂O₁₉ was used for packaging LED devices. The emission spectra of the LED device driven under a direct current of 20 to 200 mA are shown in Fig. 5(c), in which strong broadband emission of the SrGa₁₂O₁₉:Cr³⁺ phosphor mixed with minor blue emission of the LED chip that was not absorbed by the phosphor was observed. The spectral configuration of the LED device emission in Fig. 5(c) is similar to that of the SrGa₁₂O₁₉:Cr³⁺ phosphor in Fig. 1; however, the emission located at 752 nm in Fig. 5(c) differs slightly from that about 766 to 783 nm in Fig. 1, which may be due to the different ways of excitation. As shown in the

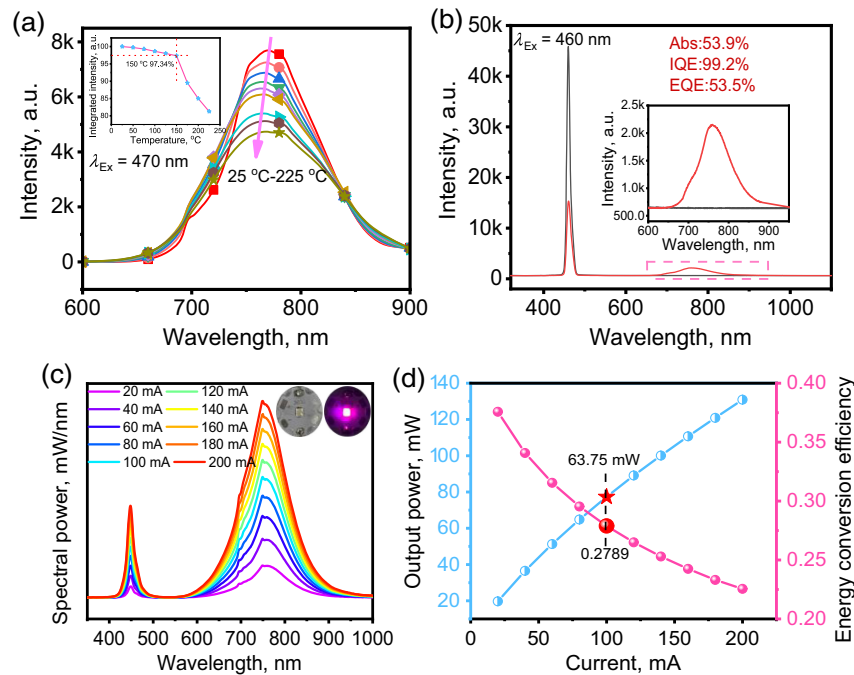


Fig. 5 (a) The thermal stability and (b) quantum efficiency of Sr(Ga_{0.99}Cr_{0.01})₁₂O₁₉ phosphor luminescence; and (c) the optical and (d) electronic properties of the NIR LED device packaged using the Sr(Ga_{0.99}Cr_{0.01})₁₂O₁₉ phosphor. (a) Emission spectra of Sr(Ga_{0.99}Cr_{0.01})₁₂O₁₉ phosphor under the excitation of 470 nm ranged from 25°C to 225°C. (b) The measurement on absorbance and internal and EQE of Sr(Ga_{0.99}Cr_{0.01})₁₂O₁₉ phosphor, in which the emission spectrum of calibration light source and the emission and reflection spectra of Sr(Ga_{0.99}Cr_{0.01})₁₂O₁₉ phosphor are listed. (c) The emission spectra of the NIR LED device packaged using the Sr(Ga_{0.99}Cr_{0.01})₁₂O₁₉ phosphor driven under different currents. (d) The output power and energy conversion efficiency of the NIR LED device as a function of current.

curve plotted in Fig. 5(d), the output power and energy conversion efficiency at 20 mA were 19.69 mW and 37.58%, respectively, and they are 77.31 mW and 27.89%, respectively, under 100 mA driving.

Finally, the potential of NIR light for photomedicine application was demonstrated by culturing the BV-2 microglia cells in our group. Under normal physiological conditions, microglial cells are in a static resting state (M0 phenotype) and play an important role in immunosurveillance. Under pathologic conditions, the microglia cells are quickly activated and accordingly, either differentiate into a pro-inflammatory M1 phenotype with neurotoxicity or into an anti-inflammatory M2 phenotype with a neuroprotective effect. In this study, the stable passaged BV-2 microglia cells were cultured and treated with different light, i.e., white light, white and NIR light, NIR light, and blackness. The expression of single nuclear cells (phagocytes) and NK cells (immune cells) was reflected in the CD14 (cluster of differentiation 14) and CD16 (cluster of differentiation 16) immunofluorescence, wherein the higher the expression of CD14 and CD16, the greater the inflammation.

In Figs. 6(a)–6(d), the first row of blue spots shows the location of microglia cells by staining cell nuclei with DAPI (4',6-diamidino-2-phenylindole), the second row of green spots shows the microglia cells by staining cells with the CD14 and CD16 antibodies, respectively, and the third row shows the merging of the first and second rows. The merged results showed that both methods successfully stained the BV-2 microglia cells.

Figure 6(a) shows the CD14-stained immunofluorescence of BV-2 microglia cultured for 24 h under variant light circumstances. As shown in Fig. 6(a), the microglia cells in the control group were mainly composed of round resting states but were simultaneously accompanied by a small amount of the amoeboid-like proinflammatory phenotype (M1) and the elongated anti-inflammatory phenotype (M2).³⁴ Thus, much intensive expression using the CD14 staining was observed in the control group. Compared with the control group, more round microglia cells were found in the NIR group, and the expression of immunofluorescence stained using the CD14 was reduced (with decreased brightness). These phenomena suggest that the NIR reduced or reversed the inflammation and exhibited an anti-inflammation effect.³⁵ However, the white group showed significantly increased CD14 expression with brighter immunofluorescence than the control group. Moreover, the microglia cells expanded in volume and became irregular in shape in the white-light circumstance. These phenomena collectively suggested that the microglia cells were overactivated by white light and possessed with increased inflammation, which were consistent with the inflammatory morphology of BV-2 microglia induced by lipopolysaccharides.^{36–38} Thus, the white light promoted M1 polarization and showed pro-inflammatory effect. By periodically alternately employing the NIR to the microglia cells that were cultured under white light, astonishingly, the CD14 expression was significantly downregulated and the cells became small and got round with fewer protrusions, as can be found by comparing the white + NIR group with the white

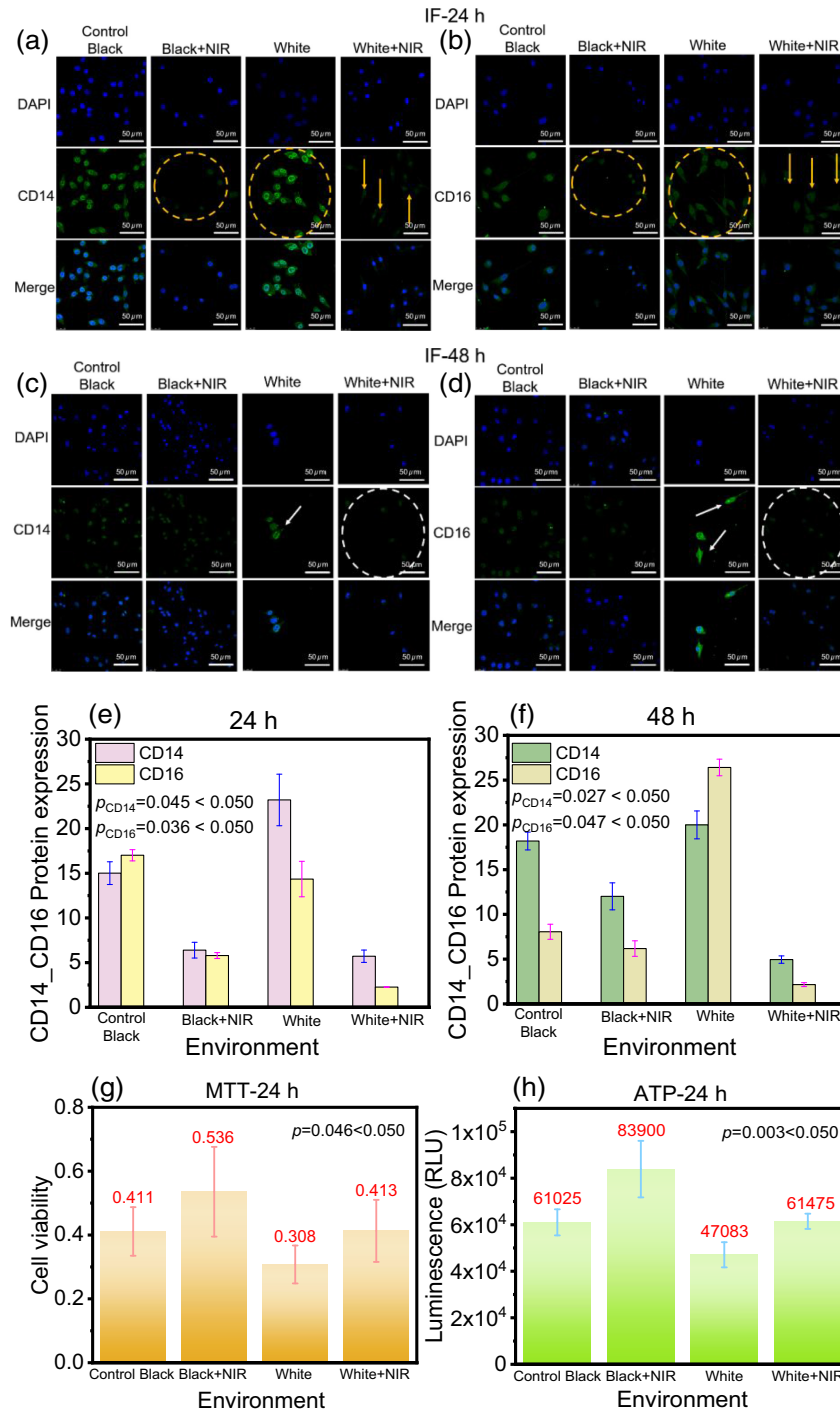


Fig. 6 Immunofluorescence detection and activity assay of BV-2 microglia under different light environments (all immunofluorescence staining is scaled to 50 μm). (a)–(d) The immunofluorescence pictures stained with the CD14 and CD16 antibodies for the microglia cultured under different light environments for 24 and 48 h, respectively; (e), (f) the expression of the CD14 and CD16 antibodies for the microglia cultured under different light environments for 24 and 48 h, respectively; (g), (h) the assays on MTT and ATP, respectively, for the microglia cultured under different light environments for 24 h.

group. These phenomena further confirmed that the NIR light had a great anti-inflammation effect by alleviating, inhibiting, or reversing inflammation.³⁹ Besides, the negative effect of white light that promoted microglia polarization and intensified

inflammation could also be discriminated by comparing the white + NIR group with the NIR group. Comparatively, the microglia cells in the NIR group were rounder than in the white + NIR group and the CD14 expression in the NIR group was far

less than that in the white + NIR group, which also underlined the positive effect of the NIR light.

Similar conclusions could be conducted from the immunofluorescence stained using the CD16 in Fig. 6(b). In comparison with the control group, the smaller size and round appearance with decreased expression in immunofluorescence were observed in the NIR group, indicating the evident anti-inflammatory effect of the NIR light.³⁵ Although the difference in immunofluorescence expression between the white group and the control group was not significant, which may be because it takes time for white light to induce microglia, the microglia cells with intensively elongated amoeba profile were observed in the white group. In contrast, the microglia cells in the control group were more regular, mainly with a round shape. The significant difference in appearance also indicated that the white light had the negative effect of being pro-inflammatory.³⁵ Moreover, the comparison of the white + NIR group with the white group showed that the introduction of NIR in white light significantly decreased the expression of CD16, and the elongated profile of cells has been evidently shortened, further confirming that the NIR light could effectively alleviate, inhibit, or even reverse inflammation.³⁹ Yet, compared with the NIR group, the cells' volume was relatively bigger and the cells' profile was irregular as far as the white + NIR group is concerned. Summing up by combining the white light and NIR light and their alternative effects, we can get to know that the white light could cause the polarization of microglia cells due to overactivation, lead to microglia deformation, and, in turn, promote inflammation. Gratifyingly, the harm caused by the white light could be repaired by the NIR through depolarization, deformations, and anti-inflammation.

With culture time extended from 24 to 48 h, the cells' immunofluorescence pictures stained with the CD14 and CD16 are shown in Figs. 6(c) and 6(d), respectively. Compared with the results shown in Figs. 6(a) and 6(b), the microglia cells in the control, NIR, and white + NIR groups in Figs. 6(c) and 6(d) all became smaller, especially for the control and the NIR groups. This is due to the accumulative effect of the NIR light on cells upon extending time, leading to the microglia cells tending to restore the M0 phenotype with a round shape. But as for the white group, the CD14 expression decreased a little while the CD16 expression increased intensively as culture time extended from 24 to 48 h, as can be discriminated by the comparisons of Fig. 6(c) with Figs. 6(a) and 6(d) with Fig. 6(b), respectively. Moreover, the microglia cells in the white group became bigger and more irregular. As the arrow marked in Fig. 6(d), the longest reached about 50 μm in size. These phenomena suggested that the white light intensified the M1 polarization of microglia cells and possibly underwent transformation from the M1 to M2 phenotype. The results in Figs. 6(c) and 6(d) not only confirmed the negative effect of white light and the positive effect of NIR light but also showed their accumulative effect on cells with prolonged time.

The statistical analysis on the immunofluorescence intensity of microglia cells, which were cultured for 24 and 48 h and stained using the CD14 and CD16, were presented in Figs. 6(e) and 6(f), respectively, in which the p values are smaller than 0.05 and have statistical significance. The introduction of NIR into black and white conditions, respectively, reduced the expression of both CD14 and CD16 simultaneously, as seen by comparing the NIR group with the control group and the white + NIR group with the white group either in Fig. 6(e)

for 24 h or in Fig. 6(f) for 48 h. The result confirmed that the NIR could attenuate microglia M1 polarization and reduce inflammation. As for the control group, the CD14 expression increased while the CD16 decreased with culture time rose from 24 to 48 h. Still, as for the white group, the relative expression of the CD14 decreased while the CD16 decreased with culture time extended from 24 to 48 h, as can be found by the comparison of Figs. 6(e) with 6(f). Such a change may be caused by the transformation of microglia cells from M1 to M2 phenotype. Since the white light has a pro-inflammation effect, along with microglia cells' prolonged exposure to white light, the inflammation would accumulate, and then microglia cells release anti-inflammatory factors. Accordingly, the microglia cells underwent a transformation from M1 to M2 phenotype and exerted the anti-inflammation effect, as can be found from the elongated cell of the white group in Fig. 6(d). As shown in Figs. 6(e) and 6(f), both the expressions of the CD14 and the CD16 in the white group were more potent than those in the white + NIR group. This was due to the pro-inflammation effect of white light. Either in Fig. 6(e) for 24 h or in Fig. 6(f) for 48 h, surprisingly, the expression of CD16 in the white + NIR group was far weaker than that of CD 14, by which we can conclude that the NIR light must have reduced inflammation and should promote the transformation of microglia cells from M1/M2 to M0 phenotype. That is also why the more petite and rounded microglia cells were observed in Figs. 6(c) and 6(d), in comparison with Figs. 6(a) and 6(b).

The immunofluorescence intensity is related to the degree of inflammation and the number of cells. To reveal the mechanism of NIR light on suppressing and reducing inflammation, the tests on MTT and ATP were performed after BV-2 cells were cultured for 24 h and irradiated with one-period dosage light. As shown in Fig. 6(g), the survival rate of the white group was the lowest, the control and white + NIR groups were nearly the same, and the highest one was the NIR group.

The results suggest that white light harmed the survival of microglia cells, while the NIR can repair the harm and reduce inflammation, as concluded by comparing the control, white, and white + NIR groups. Moreover, the survival rate of the NIR group was higher than that of the control group. Therefore, comparing the NIR group with the control group showed that the NIR light could effectively promote microglia cells' proliferation and improve microglia cells' survival rate, providing more space and possibility for regulating microglia shape and phenotype.

As shown in Fig. 6(h), the order of the ATP released by microglia under different light sources was consistent with the results of MTT proliferation and differentiation [Fig. 6(g)], where $p = 0.046$ (MTT) < 0.050 and $p = 0.003$ (ATP) < 0.050 , with highly statistical significance; that is, the ATP released by microglia under white light was the lowest, followed by the control group and the white + NIR light group, and the highest was the NIR group. The result indicated that the NIR light could promote microglia to release energy. Since ATP is a direct energy source for cellular activities, the enhanced production of ATP suggests that NIR can effectively provide energy for cell growth, which in turn offers conditions for microglia phenotype regulation and morphology restoration.⁴⁰

According to the previously reported literature, most of them chose the laser and a minority used narrowband LEDs as the light sources to study the PBM effect on microglia; the light sources, research models (targets), light dose, and therapy effect are summarized in Table 2. The highlight of this work is that we

Table 2 Summarization of previously reported literatures on regulating microglia using the PBM approach.

PBM light	Target	Dose	Effect	Refs.
632.8 nm laser	Microglia	20 J/cm ²	Attenuation of toll-like receptor-mediated pro-inflammatory responses in microglia	41
670 nm laser	Müller cell	—	Improved Müller cell-mediated microglia activation	42
670 nm laser	C57Bl/6J mice	4 J/cm ²	Neuroglia activate and modulate neuroinflammation	43
808 nm pulsed laser	Neurological injury model rats	—	Inhibition of microglia activation leading to neuroprotection	44
808 nm laser	AD model mice	25 mW/cm ² ; 3 J/cm ²	Regulates the transition of microglia and astrocytes from the M1 phenotype to the M2 phenotype	45
810 nm laser	Sprague Dawley rats	—	Regulation of microglia shift from M1 phenotype to M2 phenotype	46
10 Hz 1070 nm pulsed LED (narrow band)	AD model mice	25 mW/cm ² ; 4.5 J/cm ²	Reduces perivascular microglia and promotes angiogenesis to further enhance A β clearance	47
10 Hz 1070 nm pulsed LED (narrow band)	AD model mice	4 J/cm ²	Promoting the transformation of M1 inflammatory microglial cells into M2 anti-inflammatory types	48
1267 nm laser	Diabetic mice	37 J/cm ²	Improved effects of insulin treatment on microglia morphology and responsiveness	49
Broadband emission in the region of 600 to 950 nm with a peak at 768 nm	Microglia cells	10 mW/cm ²	Alleviate, inhibit, and reverse inflammation of microglia cells; promote microglia transforming from the overactivation M1/M2 phenotype to resting M0 phenotype; promote microglia proliferation and improve microglia survival rate	This work

used the SrGa₁₂O₁₉:Cr³⁺ phosphor-converted broadband-emitting LED as the NIR light source, whose emission wavelength nearly covers all ranges of the cytochrome c oxidase absorption (as shown in Fig. S7 in the [Supplementary Material](#)), and positive results were obtained.

4 Conclusions

In summary, a new type of NIR light source, which promisingly alleviates, inhibits, and reverses inflammation of microglia cells, promotes microglia cell proliferation, and improves microglia cells' survival rate, was demonstrated in this work. The NIR light source was fabricated using a blue LED chip and an NIR-emitting SrGa₁₂O₁₉:Cr³⁺ phosphor. The absorbance, internal, and EQE of the optimal Sr(Ga_{0.99}Cr_{0.01})₁₂O₁₉ phosphor, synthesized at 1400°C for 8 h using 1% H₃BO₃ + 1% AlF₃ as flux, are 53.9%, 99.2%, and 53.5%, respectively. The phosphor exhibits excellent thermal stability of luminescence, whose luminescence intensity at 150°C maintains 97.34% of that at room temperature. With no more than 10% mole ratio of Ba doped into SrGa₁₂O₁₉:Cr³⁺, it realizes the widening of the emission band, yet not at the expense of decreasing luminescence. The FWHM of the emission spectrum of (Sr_{0.9}Ba_{0.1})Ga₁₂O₁₉:Cr³⁺ broadens about 5 nm in contrast to that of SrGa₁₂O₁₉:Cr³⁺ without decreasing luminescence intensity. The mechanism of concentration-quenching luminescence of Cr³⁺ in the Sr(Ga_{1-x}Cr_x)₁₂O₁₉ phosphor is caused by energy transfer between near-neighbor ions. The output power and energy-conversion efficiency of the NIR LED device packaged using the SrGa₁₂O₁₉:Cr³⁺ phosphor driven at 20 mA were 19.69 mW and 37.58%, respectively. The broadband emission of the NIR LED device covered the absorption peaks of cytochrome c oxidase. Consequently, NIR light could efficiently promote the proliferation of microglia, reverse the overactivation of microglia by white light, regulate microglia from the pro-inflammatory M1

and the anti-inflammatory M2 phenotypes to the resting M0 phenotype, suppress inflammation, produce ATP, improve activity, and reduce the apoptosis of microglia. Therefore, this work provides a noninvasive approach for suppressing neuroinflammation toward neurodegenerative disease treatment, which is extremely valuable for reference and guidance to treat neurodegenerative diseases, such as PD, AD, and amyotrophic lateral sclerosis. Moreover, this study provides new clues for understanding the mechanism of PBM and the interaction between light and neurons from the cellular and molecular viewpoints of microglia. In addition, the NIR phosphor and light source reported in this work will be of interest for various applications in food safety detection, infrared imaging, infrared detection, iris recognition, and others.

Disclosures

The authors declare no conflicts of interest.

Code and Data Availability

The data sets are available from the corresponding author upon request.

Acknowledgments

This work was supported by the National Natural Science Foundation of China (Grant No. 21875058), the Natural Science Foundation of Anhui Province (Grant No. 2208085J13), the Major Science and Technology Project of Anhui Province (Grant No. 202103a05020025), the Open Foundation of National Joint Engineering Research Center for Abrasion Control and Molding of Metal Materials of Henan University of Science and Technology (Grant No. HKDNM2019015), and the Major Science and Technology Project of Zhongshan City

of Guangdong Province on the Strategic Emerging Industries Technology Research Topic, China (Grant No. 2022A1007).

References

1. Y. Hou et al., "Ageing as a risk factor for neurodegenerative disease," *Nat. Rev. Neurol.* **15**, 565–581 (2019).
2. W. Poewe et al., "Multiple system atrophy," *Nat. Rev. Dis. Primers* **8**, 57 (2022).
3. B. S. Connolly and A. E. Lang, "Pharmacological treatment of Parkinson disease: a review," *JAMA* **311**, 1670–1683 (2014).
4. Y. Park et al., "Materials chemistry of neural interface technologies and recent advances in three-dimensional systems," *Chem. Rev.* **122**, 5277–5316 (2021).
5. Z. Ni and R. Chen, "Transcranial magnetic stimulation to understand pathophysiology and as potential treatment for neurodegenerative diseases," *Transl. Neurogener.* **4**, 22 (2015).
6. E. Check, "Parkinson's patients show positive response to implants," *Nature* **416**, 666 (2002).
7. M. T. Heemels, "Neurodegenerative diseases," *Nature* **539**, 179 (2016).
8. E. Mass et al. "A somatic mutation in erythro-myeloid progenitors causes neurodegenerative disease," *Nature* **549**, 389–393 (2017).
9. P. E. MgGuff, R. A. Deterling, Jr., and L. S. Gottlieb, "Tumoricidal effect of laser energy on experimental and human malignant tumors," *N. Engl. J. Med.* **273**, 490–492 (1965).
10. E. Mester et al., "Untersuchungen über die hemmende bzw. fördernde Wirkung der Laserstrahlen," *Langenbecks Archiv für klinische Chirurgie* **322**, 1022–1027 (1968).
11. V. Heiskanen and M. R. Hamblin, "Photobiomodulation: lasers vs. light emitting diodes?" *Photochem. Photobiol. Sci.* **17**, 1003–1017 (2018).
12. L. F. de Freitas and M. R. Hamblin, "Proposed mechanisms of photobiomodulation or low-level light therapy," *IEEE J. Sel. Top. Quantum Electron.* **22**, 348–364 (2016).
13. Y. Zhang et al. "Blue LED-pumped intense short-wave infrared luminescence based on Cr³⁺-Yb³⁺-co-doped phosphors," *Light Sci. Appl.* **11**, 136 (2022).
14. S. H. Miao et al., "Broadband short-wave infrared light-emitting diodes based on Cr³⁺-doped LiScGeO₄ phosphor," *ACS Appl. Mater.* **13**, 36011–36019 (2021).
15. F. Salehpour et al., "Brain photobiomodulation therapy: a narrative review," *Mol. Neurobiol.* **55**, 6601–6636 (2018).
16. C. L. Hamilton et al., "Buckets: early observations on the use of red and infrared light helmets in Parkinson's disease patients," *Photomed. Laser Surg.* **37**, 615–622 (2019).
17. D. M. Johnstone et al., "Exploring the use of intracranial and extracranial (remote) photobiomodulation devices in Parkinson's disease: a comparison of direct and indirect systemic stimulations," *J. Alzheimer's Dis.* **83**, 1399–1413 (2021).
18. R. H. Michael and Y. Y. Huang, *Photobiomodulation in the Brain: Low-Level Laser (Light)*, Academic Press (2019).
19. D. Meder et al., "The role of dopamine in the brain: lessons learned from Parkinson's disease," *NeuroImage* **190**, 79–93 (2019).
20. G. S. Bloom, "Amyloid- β and tau: the trigger and bullet in Alzheimer disease pathogenesis," *JAMA Neurol.* **71**, 505–508 (2014).
21. C. Gonzalez et al., "Modeling amyloid beta and tau pathology in human cerebral organoids," *Mol. Psychiatry* **23**, 2363–2374 (2018).
22. M. Cowan and W. A. Petri, "Microglia: immune regulators of neurodevelopment," *Front. Immunol.* **9**, 2576 (2018).
23. T. C. Frank-Cannon et al., "Does neuroinflammation fan the flame in neurodegenerative diseases?" *Mol. Neurodegener.* **4**, 47 (2009).
24. J. Chen et al., "Inhibition of AGEs/RAGE/Rho/ROCK pathway suppresses non-specific neuroinflammation by regulating BV2 microglial M1/M2 polarization through the NF- κ B pathway," *J. Neuroimmunol.* **305**, 108–114 (2017).
25. M. K. Jha, W. H. Lee, and K. Suk, "Functional polarization of neuroglia: implications in neuroinflammation and neurological disorders," *Biochem. Pharmacol.* **103**, 1–16 (2016).
26. B. Malysa, A. Meijerink, and T. Jüstel, "Temperature dependent Cr³⁺ photoluminescence in garnets of the type X₃Sc₂Ga₃O₁₂ (X = Lu, Y, Gd, La)," *J. Lumin.* **202**, 523–531 (2018).
27. J. Xu, J. Ueda, and S. Tanabe, "Toward tunable and bright deep-red persistent luminescence of Cr³⁺ in garnets," *J. Am. Ceram. Soc.* **100**, 4033–4044 (2017).
28. M. G. Brik et al., "Spectroscopy of YAl₃(BO₃)₄: Cr³⁺ crystals following first principles and crystal field calculations," *Philos. Mag.* **90**, 4569–4578 (2010).
29. H. Xiao et al., "Cr³⁺ activated garnet phosphor with efficient blue to far-red conversion for pc-LED," *Adv. Opt. Mater.* **9**, 2101134 (2021).
30. H. Cai et al., "Tuning luminescence from NIR-I to NIR-II in Cr³⁺-doped olivine phosphors for nondestructive analysis," *J. Mater. Chem. C* **9**, 5469–5477 (2021).
31. L. Chen et al., "A new red phosphor of the Mn activated non-stoichiometric strontium aluminate 3SrO · 5Al₂O₃ for warm white light-emitting diodes," *Funct. Mater. Lett.* **6**, 1350028 (2013).
32. L. Chen et al., "A new green phosphor of SrAl₂O₄: Eu²⁺, Ce³⁺, Li⁺ for alternating current driven light-emitting diodes," *Mater. Res. Bull.* **47**, 4071–4075 (2012).
33. S. Liu et al., "Site engineering strategy toward enhanced luminescence thermostability of a Cr³⁺-doped broadband NIR phosphor and its application," *Mater. Chem. Front.* **5**, 3841–3849 (2021).
34. H. X. Xiao et al., "Paraquat mediates BV-2 microglia activation by raising intracellular ROS and inhibiting Akt1 phosphorylation," *Toxicol. Lett.* **355**, 116–126 (2022).
35. J. Melief et al., "Phenotyping primary human microglia: tight regulation of LPS responsiveness," *Glia* **60**, 1506–1517 (2012).
36. M. Ban et al., "An active fraction from *Spatholobus suberectus* dunn inhibits the inflammatory response by regulating microglia activation, switching microglia polarization from M1 to M2 and suppressing the TLR4/MyD88/NF- κ B pathway in LPS-stimulated BV₂ cells," *Heliyon* **9**, e14979 (2023).
37. J. Li et al., "Edaravone plays protective effects on LPS-induced microglia by switching M1/M2 phenotypes and regulating NLRP3 inflammasome activation," *Front. Pharmacol.* **12**, 691773 (2021).
38. Q. Cao et al., "Production of proinflammatory mediators in activated microglia is synergistically regulated by Notch-1, glycogen synthase kinase (GSK-3 β) and NF- κ B/p65 signalling," *PLoS One* **12**, e0186764 (2017).
39. N. Viceconte et al., "Neuromelanin activates proinflammatory microglia through a caspase-8-dependent mechanism," *J. Neuroinflammation* **12**, 5 (2015).
40. J. L. Wilson et al., "Carbon monoxide reverses the metabolic adaptation of microglia cells to an inflammatory stimulus," *Free Rad. Bio. Med.* **104**, 311–323 (2017).
41. S. Song, F. Zhou, and W. R. Chen, "Low-level laser therapy regulates microglial function through Src-mediated signaling pathways: implications for neurodegenerative diseases," *J. Neuroinflammation* **9**, 219 (2012).
42. Y. Z. Lu et al., "Photobiomodulation with 670 nm light ameliorates Müller cell-mediated activation of microglia and macrophages in retinal degeneration," *Exp. Eye Res.* **165**, 78–89 (2017).
43. S. Saieva and G. Tagliabue, "Near-infrared light reduces glia activation and modulates neuroinflammation in the brains of diet-induced obese mice," *Sci. Rep.* **12**, 10848 (2022).
44. R. O. Esenaliev et al., "Nano-pulsed laser therapy is neuroprotective in a rat model of blast-induced neurotrauma," *J. Neurotrauma* **35**, 1510–1522 (2018).
45. L. Yang et al., "Non-invasive photobiomodulation treatment in an Alzheimer disease-like transgenic rat model," *Theranostics* **12**, 2205 (2022).

46. J. W. Song et al., "Low-level laser facilitates alternatively activated macrophage/microglia polarization and promotes functional recovery after crush spinal cord injury in rats," *Sci. Rep.* **7**, 620 (2017).
47. L. Tao et al., "Microglia modulation with 1070-nm light attenuates A β burden and cognitive impairment in Alzheimer's disease mouse model," *Light Sci. Appl.* **10**, 179 (2021).
48. C. Chen et al., "Exosomes derived from M2 microglial cells modulated by 1070-nm light improve cognition in an Alzheimer's disease mouse model," *Adv. Sci.* **10**, 2304025 (2023).
49. S. Liu et al., "Transcranial photobiomodulation improves insulin therapy in diabetic microglial reactivity and the brain drainage system," *Commun. Biol.* **6**, 1239 (2023).

Qi Liu is currently a master's student at the School of Materials Science and Engineering, Hefei University of Technology. He is mainly engaged in NIR phosphor research for PBM application, including LED device packages and cell and animal experiments, using self-developed NIR light.

Bo Wang is currently an associate professor in the Wuyi University (Jiangmen). He received his bachelor's degree from the Northwestern Polytechnical University in 2012 and received his PhD from Fujian Institute of Research on the Structure of Matter, Chinese Academy of Sciences, in 2017. His current research interests mainly include synthesis of luminescent materials for solid-state lighting and multifunctional composite materials.

Lei Chen is currently a professor at the School of Materials Science and Engineering, Hefei University of Technology. He has been engaged in lighting and display research for long time. Presently, he mainly takes the interdisciplinary researches on luminescence, optometry, and brain science, particularly on developing advanced therapy technologies and medical instrument for children and adolescent myopia and the aged Parkinson's and Alzheimer's diseases using the non-invasive photobiomodulation approach.

Biographies of the other authors are not available.